ACS APPLIED MATERIALS & INTERFACES

Research Article

www.acsami.org

Ionic Liquid-Silica Precursors via Solvent-Free Sol−Gel Process and Their Application in Epoxy-Amine Network: A Theoretical/Experimental Study

Magdalena Perchacz,*[†] Ricardo Keitel Donato,[‡] Leandro Seixas,[‡] Alexander Zhigunov,[†] Rafał Konefał,[†] Magdalena Serkis-Rodzeń,[†] and Hynek Beneš[†]

[†]Institute of Macromolecular Chemistry AS CR, v.v.i., Heyrovsky Sq. 2, 162 06 Prague 6, Czech Republic

[‡]MackGraphe—Graphene and Nanomaterials Research Center, Mackenzie Presbyterian University, Rua da Consolação 896, São Paulo 01302-907, SP Brazil

Supporting Information

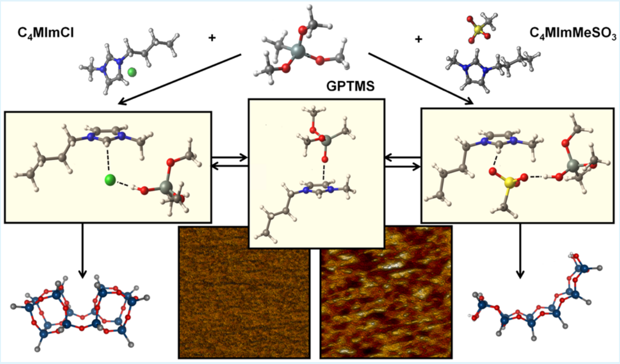

ABSTRACT: This work describes the solvent-free sol−gel synthesis of epoxy-functionalized silica-based precursors in the presence of 1-butyl-3-methylimidazolium-based ionic liquids (ILs) containing different anions: chloride (Cl^-) and methanesulfonate ($MeSO_3^-$). The IL-driven sol−gel mechanisms were investigated in detail using experimental characterizations (^{29}Si NMR and ATR FTIR spectroscopy) and a theoretical computational method based on density functional theory (DFT). We observed complex IL influence on both hydrolysis and condensation steps, involving especially H-bonding and Coulomb coupling stabilization of the process intermediates. The obtained IL−silica precursors and their further xerogels were widely characterized (rheology measurements, MALDI TOF, ^{29}Si NMR, ATR FTIR, and DFT simulation), which allowed observation of their precise silica structures and established their most energetically favorable conformations. The detected silica structures were dependent on the IL type and varied from highly condensed 3D cage-like to branched ladder-like and cyclic ones. The application of prepared IL−silica precursors as reinforcing additives into the epoxy−amine network led to an improvement in the organic/inorganic interphase interactions through chemical and physical bonding. Uniform and well-dispersed silica aggregates, in the size of ~30 nm, were formed when ≤6.8 wt % of each IL−silica precursor was applied into the epoxy−amine network. The use of imidazolium-based ILs contributed to a significant improvement in thermomechanical properties of hybrids and reduced their UV absorption ability compared to that of the reference matrix. All hybrids exhibited an increase in energy to break (up to ~53%), elongation at break (up to ~43%), shear storage modulus in the rubbery region (up to 4 times), and thermo-oxidative stability.

KEYWORDS: *sol−gel process, imidazolium ionic liquid, 3D POSS structures, IL−silica precursor, epoxy−silica hybrid material*

1. INTRODUCTION

Recently, epoxy−silica hybrid materials based on epoxy matrix and dispersed silica domains of various shapes and architectures have been broadly studied.[1−11] Such intensive investigations were driven by the outstanding properties of inorganic silica phase which, through the combination of hardness and thermal and chemical stability with toughness, flexibility, and easy organic phase processability, allow tailoring of the final material properties.[12,13]

The well-known route of epoxy−silica hybrid preparation involves physical incorporation of differently shaped silica nanoparticles (spherical SiO_2, POSS cages, etc.) into an epoxy resin.[14−17] Nevertheless, an increase in viscosity and energy-intensive filler dispersion, resulting in formation of silica aggregates and heterogeneities in the final hybrid, are two major drawbacks of this approach. Therefore, the sol−gel process of various alkoxysilanes enabling in situ formation of silica species during epoxy cross-linking has been broadly examined.[2,4−7,12,13,18−21] However, volatile byproducts such as water and alcohols formed during hydrolysis/condensation of alkoxysilane as well as solvents added in the conventional sol−gel process made difficult the preparation of bulky materials. According to the latter, a nonhydrolytic sol−gel of alkoxysilanes allowing preparation of massive epoxy−silica hybrids (as no water and cosolvents are needed) was developed.[8,9] Nevertheless, this method requires usage of relatively high amount of expensive catalyst, which then causes aggregation of silica particles. Therefore, another solution might be the solvent-free

Received: February 22, 2017
Accepted: April 26, 2017
Published: April 26, 2017

DOI: 10.1021/acsami.7b02631

sol−gel process consisting of the ex situ hydrolysis/condensation of alkoxysilanes with under-stoichiometric amount of added water.[10,22,23] The resulted liquid silica-based precursors (sols) are easily incorporated into the epoxy network in their precondensed form, which helps avoiding formation of volatiles.

Much interest has been put to the use of functionalized alkoxysilanes bearing, e.g., epoxy or amino groups able to covalently bond with the organic matrix and increase organic/inorganic (O/I) phase compatibility.[3,8−10] Accordingly, we significantly improved the thermomechanical properties of glassy epoxy−amine matrix by addition of silica-based precursors, which were prepared using the solvent-free sol−gel process of (3-glycidyloxypropyl)trimethoxysilane (GPTMS).[10] It was also proved that the structure of formed silica species might be modified using different types of catalysts.[23] Moreover, the epoxy-functionalized side-chain of formed silica structures allowed chemical bonding with the organic network, which led to the better compatibility between both phases. Nevertheless, the addition of silica-based precursors was limited to ∼3.6 wt %, as the formation of large aggregates was observed at higher precursor loadings.[10] Therefore, based on previous research,[5−7] we assumed that the incorporation of ionic liquids (ILs) would help to improve the O/I interphase interactions and reduce the nanofiller aggregation tendency.

In general, ILs exhibit several desirable properties, e.g. negligible vapor pressure, nonflammability even at higher temperatures, moderate polarity and surface tensions, wide range of conductivities, and high thermal stability, which make them suitable additives for polymers.[24−26] The imidazolium-based ILs are the most frequently used, as they found various applications in batteries, catalysis, fuel cells, ionogel chemistry, lubrication, electrochemistry, materials science, etc.[24−29] The unique properties of each IL depend on dominant Coulombic ion−ion interactions, characteristic H-bonding, $\pi-\pi$ stacking of the rings, and van der Waals forces. Thus, in many ILs, cations and anions form hydrogen-bonded nanostructural 3D supramolecular networks. Moreover, IL solutions create complex and concentration-dependent structures, e.g. supramolecular aggregates, contact ion pairs, and triple ions.[24,30,31]

Lately, the imidazolium ILs have been used in the sol−gel process as multifunctional additives able to catalyze the hydrolytic polycondensation reaction.[32,33] According to the literature,[28,34−38] the imidazolium ring's hydrogens possess acid nature and can protonate alkoxysilanes, promoting their hydrolysis. Moreover, the hydrogen bonding between water molecules and IL anions, which are Lewis bases, could deprotonate formed silanols and accelerate their condensation to Si−O−Si bonds.

Using the fact that imidazolium ILs can interact with silica species, forming homogeneous materials with tailored morphologies, we investigated their influence on the preparation and properties of epoxy−silica hybrid materials. At first, the role of 1-butyl-3-methylimidazolium chloride (C_4MImCl) and 1-butyl-3-methylimidazolium methanesulfonate ($C_4MImMeSO_3$) in the sol−gel process of (3-glycidyloxypropyl)trimethoxysilane (GPTMS) was studied in detail, crossing the experimental Fourier transform infrared spectroscopy (ATR FTIR) and silicon-29 nuclear magnetic resonance (^{29}Si NMR) results with density functional theory (DFT) simulations of the silica−IL interactions. Moreover, the silica-based precursors were characterized by matrix-assisted laser desorption/ionization time-of-flight mass spectrometry (MALDI TOF), small-angle X-ray scattering (SAXS), and rheological measurements, and the formed silica structures were confirmed by DFT method. Afterward, the obtained highly condensed silica-based products were applied into a glassy epoxy−amine network to investigate their effect on morphology and thermomechanical properties of epoxy−silica hybrids. The final hybrid materials were characterized by SAXS, atomic force microscopy (AFM), ultraviolet−visible spectroscopy (UV−vis), dynamic mechanical and thermal analysis (DMTA), tensile testing and thermogravimetric analysis (TGA).

The aim of this work was to better understand the IL's role (i.e., template, catalyst, etc.) in the sol−gel process as well as to obtain homogeneous, highly condensed, easy miscible with epoxy resin, and highly storage stable silica-based precursors. The use of ILs could lead to long shelf life nanosilica additives with controlled structure and morphology, which strongly influence the properties of the epoxy-based materials to which they are applied.

2. EXPERIMENTAL SECTION

2.1. Synthetic Procedures.

2.1.1. Synthesis of Silica-Based Precursors and Xerogels. The two silica-based precursors bearing functional epoxide groups were synthesized using the two-stage closed sol−gel system, as described previously.[23] Briefly, GPTMS (98%, ABCR) was prehydrolyzed at room temperature in the presence of distilled water ($H_2O/Si\text{-}OCH_3 = 0.42$) and two commercially available imidazolium ILs (IL/GPTMS = 0.01), 1-butyl-3-methylimidazolium chloride (C_4MImCl, 99%, IOLITEC) and 1-butyl-3-methylimidazolium methanesulfonate ($C_4MImMeSO_3$, 99%, IOLITEC), and further polycondensed under reflux at 80 °C. The ILs were characterized using DSC and TGA (Figure S1 and Table S1), by which the melting (T_m), glass transition (T_g), and thermal degradation (T_{max} − DTG peak) temperatures of C_4MImCl ($T_m = 49.5$ °C; $T_g = -52$ °C; $T_d = 310$ °C) and $C_4MImMeSO_3$ ($T_m = 65.8$ °C; $T_g = -57$ °C; $T_{max} = 406$ °C) were determined. The relaxed chemical structures of both ILs are shown in Figure 1.

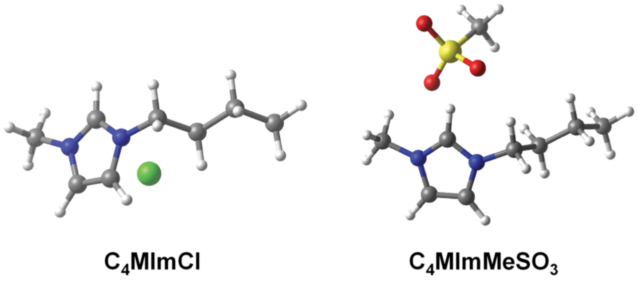

Figure 1. Relaxed chemical structures of the ILs used in this work (legend of atoms: C, gray; H, white; N, blue; S, yellow; O, red).

To control the kinetics of hydrolytic polycondensation reactions, the sol fractions were collected in equal intervals and analyzed using ATR FTIR spectroscopy. The sol−gel process was stopped when no significant changes in Si−O−Si region from ca. 900−1200 cm^{-1} in IR spectra were visible. Such inhibition of polycondensation might be due to reaching the mixture equilibrium, triggered by the formation of side-product (methanol), which stayed in the reaction system. At this point, the rheology and the condensation degree of the prepared precursors were measured using DMTA and ^{29}Si NMR, respectively.

The samples were kept in a refrigerator at 8 °C, and their homogeneity, solubility in THF, and changes in viscosity were recorded with time to determine their storage stability. The gel point was characterized as the time of first insoluble fraction appearance. The obtained xerogels were dried (vacuum oven, 70 °C, 3 h), crushed in a mortar, and characterized (ATR FTIR, ^{29}Si MAS NMR and SAXS).

2.1.2. Preparation of Epoxy−Silica Hybrids. The epoxy−silica hybrid networks were prepared at stoichiometric molar ratio of epoxide groups from a diglycidyl ether of bisphenol A (DGEBA, D.E.R. 332, The Dow Chemical Company, EEW = 171 g/mol) and silica-based precursor, and NH groups from cross-linking agent: poly(oxypropylene)diamine (D-230, Jeffamine D-230, Huntsman). Initially, the silica-based precursor (in the amounts of 0.5, 0.9, 1.8, 3.6, 6.8, 12.5, and 22.0 wt %) was homogenized with DGEBA resin for 20 min at 600 rpm. Then, the amine cross-linking agent (D-230) was added into the system, and the mixture was stirred (room temperature, 1000 rpm) under vacuum (30 min at 100 mbar and 30 min at 3 mbar). Finally, the reactive mixture was poured into PTFE molds and cured for 2 h at 90 °C and 20 h at 130 °C, followed by 12 h postcuring at 180 °C under vacuum.

The reference epoxy−amine matrix was prepared in a way similar to that of the epoxy−silica hybrids. The mixture containing stoichiometric molar ratio (epoxy/NH groups = 1/1 mol) of DGEBA and Jeffamine D-230 was homogenized and cured in the same temperature regime as the epoxy−silica hybrids and postcured at 180 °C for 5 h under vacuum.

To simplify the results interpretation, the studied hybrid systems were denoted according to the type of used IL (C_4MImCl, C_4MImMeSO$_3$) and the amount of silica precursor added (0.5, 0.9, 1.8, 3.6, 6.8, 12.5, and 22.0 wt %). For example, DGEBA-D-230-C_4MImCl(6.8) corresponds to the epoxy−silica hybrid material composed of DGEBA resin, D-230 hardener, and 6.8 wt % of C_4MImCl−silica precursor.

2.2. Methods. *2.2.1. Silica Structure Modeling.* The computational approaches to study the structural properties were based on DFT[39,40] as implemented in Siesta code.[41] Double-ζ localized basis and polarization orbitals (DZP), Troullier−Martins pseudopotentials,[42] mesh cutoff of 300 Ry, and exchange-correlation function in generalized-gradient approximation with Perdew−Burke−Ernzerhof parametrization (PBE)[43] were used to calculate electronic densities. All relaxations were performed with maximal forces of 0.04 eV/Å. The molecules were relaxed under simulated vacuum conditions within a 125 nm^3 cubic cell. The stretching effects were eliminated by considering distances and bond angles at the equilibrium. For binding energy calculations, a mesh cutoff of 600 Ry, relaxation with maximal forces of 0.02 eV/Å, and a 27 nm^3 cubic unit cell were used.

To calculate the binding energies between the two subsystems A and B, we calculated the total energy of the system A+B and subtracted the total energies of each separate subsystem. Thus, the binding energy

$$E_b(A, B) = E_{tot}(A + B) - E_{tot}(A) - E_{tot}(B) \quad (1)$$

provides a measure of how much energy is needed to separate the system into two parts. Negative values mean attractive interactions.

2.2.2. Infrared Spectroscopy. The ATR FTIR spectra of the products were measured using a Spectrum 100 spectrometer (PerkinElmer, United States) equipped with a mercury−cadmium−telluride (MCT) detector and universal ATR accessory with a diamond prism. Spectral resolution was 4 cm^{-1} with 16 scans taken for each spectrum.

2.2.3. Nuclear Magnetic Resonance. Solid-State ^{29}Si MAS NMR. The solid-state ^{29}Si MAS NMR experiments were measured at 11.7 T with a Bruker Avance 500 WB/US NMR spectrometer at frequency of 99.325 MHz, using double-resonance 4 mm probehead. The ^{29}Si MAS NMR spectra were performed at a spinning frequency $\omega_r/2\pi = 5$ kHz; 90° pulse width at 62.5 kHz; recycle delay of 7 s; and number of scans: 1024. The spectra were referenced to M_8Q_8 (−109.8 ppm). During detection, a high-power dipolar decoupling (TPPI) was used to eliminate strong heteronuclear dipolar coupling.

To compensate frictional heating of the spinning samples, all NMR experiments were measured under active cooling, and the sample temperature was maintained at 305 K. Precise temperature calibration was performed on Pb(NO$_3$)$_2$ using a calibration procedure described in the literature.[44]

The relative amount of structural units (T_n) was obtained from the ^{29}Si MAS NMR spectra integration. The condensation degree of alkoxy−silicone bonds (q) in prepared precursors was determined according to the following equation:

$$q = \sum_{n=1}^{3} \left(\frac{nT_n}{3} \right) \quad (2)$$

where T_n is the percentage of GPTMS structures and n is the degree of conversion of an alkoxysilane compound.

The assignment of NMR bands was as follows: T_0 from −42 to −43 ppm, T_1 from −50 to −51 ppm, T_2 from −56 to −61 ppm, and T_3 from −63 to −71 ppm.

Liquid-State ^{29}Si NMR. The ^{29}Si NMR spectra were recorded at 119.25 MHz on a Bruker Avance III 600 spectrometer at 295 K using deuterated THF as a solvent. The spectra were recorded using a spin-lock polarization experiment.[45] To decrease the interfering glass sample tube signal, a 5 mm Fluoropolymer Liner (Norell) was used. The value for 90° pulse was 8.5 μs with 8500−10000 scans, and the delay between scans was 5 s. For all the experiments, a deuterated THF solution of chromium(III) acetylacetonate (Cr(acac)$_3$) was added to shorten the relaxation time of the ^{29}Si nuclei, thus allowing quantitative spectral accumulation with the 5s delay.[46]

Liquid-State ^{1}H NMR. ^{1}H NMR spectra were acquired with Bruker Avance III 600 spectrometer operating at 600.2 MHz. The standard program of 90° pulse was used: 16 scans, 2.18 s acquisition time, 10 μs pulse width, and relaxation delay between 10 s scans. Reaction mixtures were measured in standard 5 mm NMR tubes. Acetone-d$_6$ was used as an external solvent in a capillary dropped inside a tube.

2.2.4. Viscosity and Rheology Measurements. Viscosity and rheology measurements of the IL−silica precursors were performed using Ares G2 rheometer (TA Instruments, USA). The complex viscosity (η^*, dynamic shear storage (G') and loss (G'') moduli were measured at 25 °C on a plate/plate geometry (25 mm) and at angular frequency from 100 to 0.1 rad/s.

2.2.5. MALDI TOF Mass Spectrometry. MALDI TOF mass spectra were acquired with an Ultraflex (Bruker Daltonics, Bremen, Germany) in the positive ion reflection mode using delayed extraction. The spectra were the sum of 30 000 shots with a DPSS, Nd: YAG laser (355 nm, 1000 Hz). External calibration was used.

The samples were prepared by the dried droplet method. Solution of the sample (10 mg/mL), the DHB (2,5-dihydroxybenzoic acid; 20 mg/mL) matrix and the sodium trifluoroacetate (NaCF$_3$COO; 10 mg/mL) cationization agent were mixed in THF in the respective volume ratio 4:20:1.1 μL. The mixture was deposited on a ground-steel target plate, and the analyte drop was dried at ambient atmosphere.

2.2.6. Small-Angle X-ray Scattering. The SAXS experiments were performed using a pinhole camera (Molecular Metrology SAXS System) attached to a microfocused X-ray beam generator (Osmic Micro-Max 002) operating at 45 kV and 0.66 mA (30 W). The camera was equipped with a multiwire gas-filled detector with an active area diameter of 20 cm (Gabriel design). Two experimental setups were used to cover the q range of 0.04−11 nm $^{-1}$. Scattering vector $q = (4\pi/\lambda)\sin\theta$, where $\lambda = 0.154$ nm is the wavelength, and θ is the angle between the incident X-ray beam and the detector measuring the scattered intensity.

2.2.7. Atomic Force Microscopy. Morphology of epoxy/silica hybrid materials and dispersion of admixed silica species was investigated by atomic force microscopy (Dimension Icon, Bruker) equipped with the SSS-NCLR-20 probe (Super Sharp Silicon SPM-Sensor from NanoSensors Switzerland; spring constant: 35 N·m^{-1}, resonant frequency: ≈ 170 kHz, tip radius: 2 nm) using tapping mode AFM technique. The samples of hybrids were freeze-fractured in liquid nitrogen to avoid the covering of silica particles by the polymer layer. The silica particle size was measured by NanoScope Analysis Software via section analysis.

2.2.8. UV−vis Spectroscopy. A UV−vis spectrophotometer (Lambda 950, PerkinElmer) with the 60 mm integrating sphere accessory was used to measure the scattering transmittance of the epoxy−silica hybrid materials in the visible light region using the

Table 1. Experimental Conditions of the GPTMS-Based Sol−Gel Process[a] and IL−Silica Precursors Characteristics

type of IL	amount of IL (wt %)	H_2O/Si-OCH_3 (mol/mol)	reaction time (h)[b]	dynamic viscosity (mPa·s)[c]	storage stability (days)[d]
C_4MImCl	1.0	0.4	6.0	8000	6
C_4MImMeSO_3			30.0	2200	152

[a] Reaction temperature: 80 °C; weight of GPTMS 2 g. [b] Determined from ATR FTIR measurements. [c] Viscosity at 25 °C measured after residual volatile removal (vacuum oven; 70 °C; 2 h). [d] Gel time estimated after sample storage at 8 °C.

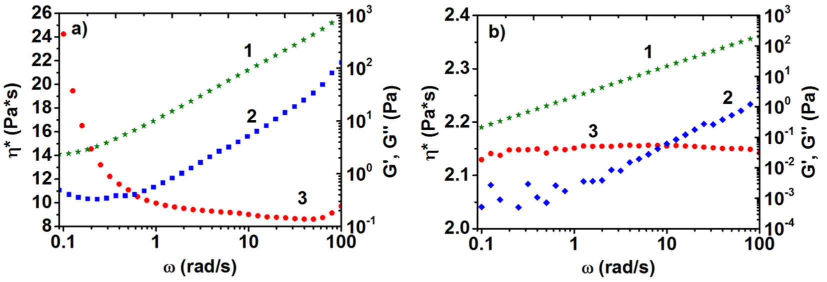

Figure 2. Rheology of C_4MImCl− (a) and C_4MImMeSO_3−silica precursors (b): (1) dynamic loss modulus, (2) dynamic storage modulus, and (3) complex viscosity.

Table 2. Distribution of *T* Species and the Total Condensation Degree of Si-OCH_3 Groups (q) of IL−Silica Precursors and Final Xerogels

		%						
type of IL	type of product	T_0	T_1	T_{2c}	T_2	T_{3c}	T_3	q
C_4MImCl	precursor	0.4	3.3	9.8	12.2	27.3	47.0	90.1
	xerogel					24.4	75.6	100
C_4MImMeSO_3	precursor	5.5	19.8	3.2	17.5	12.0	42.0	74.4
	xerogel		0.5		9.4	33.6	56.5	96.1

scanning speed of 150 nm·min^{-1} and the measuring wavelength range of 250−800 nm. The size of each square sample was approximately 15 × 15 × 1 mm.

2.2.9. Dynamic Mechanical and Thermal Analysis. The dynamic mechanical and thermal properties were tested on ARES G2 rheometer (TA Instruments). The temperature dependence of the complex shear modulus of rectangular samples (dimension: 20 × 10 × 1.5 mm^3) was measured by oscillatory shear deformation at a frequency of 1 Hz and a heating rate of 3 °C·min^{-1} in a temperature range of 25−180 °C. The rubbery storage shear modulus (G'_R) was determined in the rubbery plateau region at T = 150 °C. The temperature of main (α) transition (T_α) was evaluated as the maximum of tan δ peak. The typical precision of the measurements was $T_\alpha \pm 2$ °C and $G'_R \pm 5\%$.

2.2.10. Thermogravimetric Analysis. The thermal stability of hybrids was determined from TGA performed on a Pyris 1 TGA instrument (PerkinElmer). The weight loss was measured under oxidizing atmosphere (air) in a platinum pan using a heating rate of 10 °C·min^{-1} up to ~900 °C. The total amount of solid residues from each sample was determined at 860 °C.

2.2.11. Tensile Properties. Tensile tests were carried out on an Instron 6025 instrument (High Wycombe) at room temperature and at a test speed 1 mm·min^{-1}. At least nine "dog-bone" shaped specimens (EN ISO 527-2) with the dimensions 89 × 5 × (1.5 ± 0.2) mm^3 were tested from each system, and the final value was an average from at least 5 measurements. The Young modulus, tensile strength, energy to break, and elongation at break were evaluated.

2.2.12. X-ray Fluorescence (XRF). The samples were analyzed using an X-ray fluorescence spectrometer SPECTRO XEPOS (SPECTRO Analytical Instruments, Germany) equipped with a silicon drift detector and excitation system with a 50 WPd anode X-ray tube and three polarization secondary targets. HOPG crystal as BRAGG polarizer was used for determination of Si content. The 1 mm-thick layer of the sample was deposited on an aluminum foil (0.03 mm thick), placed into a measuring chamber, and directly irradiated. The chamber was flushed with He during the sample measurement (time: 600 s). The Spectro Xepos software (TurboQuant method) was used for data analysis. Each sample was measured 5 times to obtain the average silicon content.

3. RESULTS AND DISCUSSION

3.1. Preparation and Characterization of IL−Silica Precursors and Xerogels. The two amphiphilic 1-butyl-3-methylimidazolium-based ILs with different anions (Cl^- and $MeSO_3^-$) (Figure 1) were chosen to investigate their influence on the sol−gel kinetics of GPTMS and compare them with previous results relating to the conventionally catalyzed sol−gel process.[23] The reaction conditions and the final properties of obtained silica-based precursors were presented in Table 1.

We observed that under the same reaction conditions, C_4MImCl promoted formation of more viscous and less storage stable product in a shorter reaction time compared to C_4MImMeSO_3 (Table 1). Such behavior might signify different catalytic ability of each IL depending on the anion's type and is discussed in detail in the next subsection.

The IL−silica precursors were further characterized by dynamic shear measurements (Figure 2). In both systems, G'' dominated over G' in the whole frequency range, which is a characteristic behavior of viscous liquids (sols).[47] Nevertheless, the C_4MImCl−silica precursor displayed the formation of low-frequency plateau of G' and G'' values and a huge increase of η^*, which might indicate the presence of more condensed silica structures and probably the formation of a physical network (Figure 2a). In contrast, the C_4MImMeSO_3−silica precursor showed the significantly lower η^* values (~3.6 times) and typical Newtonian liquid behavior of η^*, i.e., frequency-independent as well as a frequency dependence of $G' \sim \omega^2$

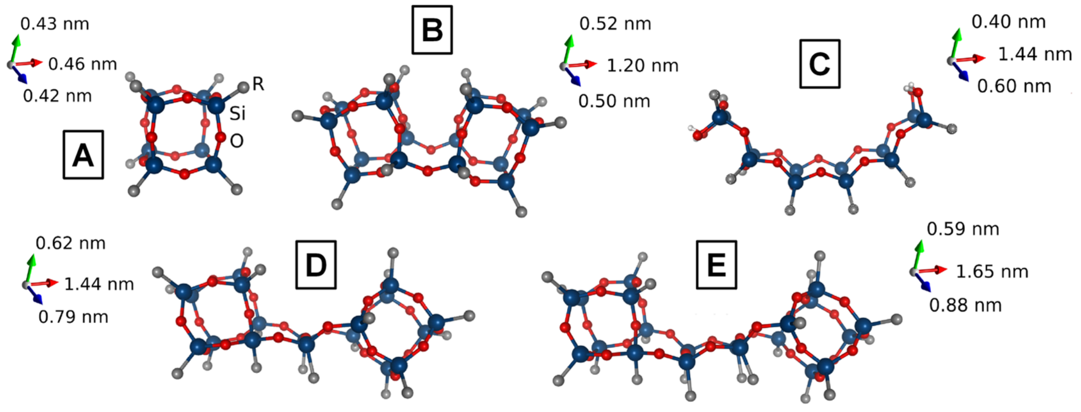

Figure 3. Proposed relaxed POSS structures present in the final xerogels, as predicted by DFT simulations: A, cage-like structure; B, D, and E, extended cage-like structures; C, ladder-like structure. Si atom (blue), O atom (red), and $-CH_2$ group (gray). (To decrease the relaxation steps and facilitate the structure visualization, the glycidyloxypropyl side chains in the structures were replaced by methyl groups.)

and $G'' \sim \omega$ (Figure 2b), indicating the presence of small segregated silica structures. The rheology results were in agreement with those summarized in Table 1, showing longer synthesis and gel time of the $C_4MImMeSO_3$−silica precursor.

The influence of IL on the type of formed silica structures was followed by ^{29}Si NMR spectroscopy (Figure S2). The condensation degree was determined using eq 2, and the detailed distributions of T species were given in Table 2.

It became evident that C_4MImCl promoted the formation of more condensed IL−silica precursor, as the peaks areas, corresponding to the T_3 and T_{3c} species, were broader, and the distribution of T_0 and T_1 species was lower than those for the $C_4MImMeSO_3$−silica precursor (Figure S2 and Table 2).

The C_4MImCl−silica precursor exhibited a high condensation degree (q = ~90%) and was mostly composed of T_3 (ca. 74%) species (Table 2), suggesting the predominant formation of 3D POSS silica structures in the sol−gel process.[43] The MALDI TOF spectrum of C_4MImCl−silica precursor showed that, besides the partially opened cage-like silica structures, also some small cyclic and short ladder-like structures were formed (Figure S3a). The observed low amount of T_1 (− 50.5 ppm) species (Table 2) probably referred to the silica end-capped and/or side-chain groups bonded to the main structures (e.g., 4, 5, 9, 11, and 14−18 in Table S2), as no linear oligomers were detected. Also, the bicondensed species (T_2 and T_{2c}) might correspond to the silicon atoms localized at the corners of ladder-like or partially opened cage-like silica structures (e.g., 2, 3, 10, and 13 in Table S2).[23] In contrast, the $C_4MImMeSO_3$−silica precursor exhibited lower condensation degree ($q \sim$ 74.4%) (Table 2). The formed silica structures were similar to those in the C_4MImCl−silica system but revealed broader size and shape distribution (see MALDI TOF spectrum in Figure S3b). Herein, the formation of cage-like (e.g., 10, 11, 13, 14, and 18 in Table S2) as well as various ladder-like and cyclic silica structures was detected (e.g., 3−6, 17, and 19−21 in Table S2), which corresponded well to the NMR results (Table 2).

The ^{29}Si MAS NMR results indicated a high condensation degree (96−100%) for both xerogels (Figure S4a and b). Accordingly, in the C_4MImCl−silica xerogel, only the fully condensed T_{3c} and T_3 species at −66 ppm and in the region between −62 and −70 ppm, respectively, were detected (Figure S4a). On the basis of these results, we predicted (using DFT simulation) the most probable silica structures in their relaxed state, as shown in Figure 3. The structures A, B, D, and E (Figure 3) could be formed in the C_4MImCl−silica xerogel, as the T_2 and T_1 species were not detected in the NMR spectrum (Figure S4a and Table 2). In contrast, in the $C_4MImMeSO_3$−silica xerogel, the formation of T_3, T_2, and T_1 species was observed (Figure S4b and Table 2), and the fully condensed siloxane units presented ~90% of conversion. Thus, mainly 3D POSS structures but also a low amount of cyclic siloxanes (as shown in Figure 3) might be formed.[23,48]

The most rigid cage-like structures (A and B in Figure 3) presented less relaxation steps, consequently producing fewer distortions from their stretched conformations. On the other hand, with increasing the planarity, the final ladder-like and extended cage-like structures suffered considerable distortion (structures C, D, and E in Figure 3), producing a significant curvature especially in the case of the ladder-like structure (structure C in Figure 3).

The presence of connected POSS structures (Figure 3d and e) in both silica xerogels was confirmed by SAXS (Figure 4).

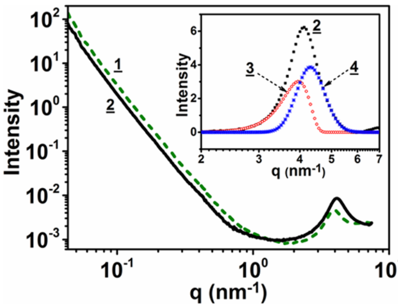

Figure 4. SAXS patterns of xerogels obtained from the C_4MImCl− (1) as well as the $C_4MImMeSO_3$−silica precursors (2) with the deconvolution of signal detected in the latter (inserted graph).

The scattering curve of C_4MImCl−silica xerogel showed the characteristic peak at q = 3.96 nm^{-1}, originating from partial ordering of silica cages (repeating distance of approximately 1.59 nm according to the Bragg's equation: $d = 2\pi/q$) (Figure 4, peak 1). A similar but only slightly broader peak was observed for the $C_4MImMeSO_3$−silica xerogel (q = 4.18 nm^{-1}), which consisted of two functions, as revealed by deconvolution (inset in Figure 4, peak 2). The position and width of the left deconvoluted peak (Figure 4, peak 3) repeated the behavior (center position and width) of a signal detected in the C_4MImCl-catalyzed xerogel and signified the presence of

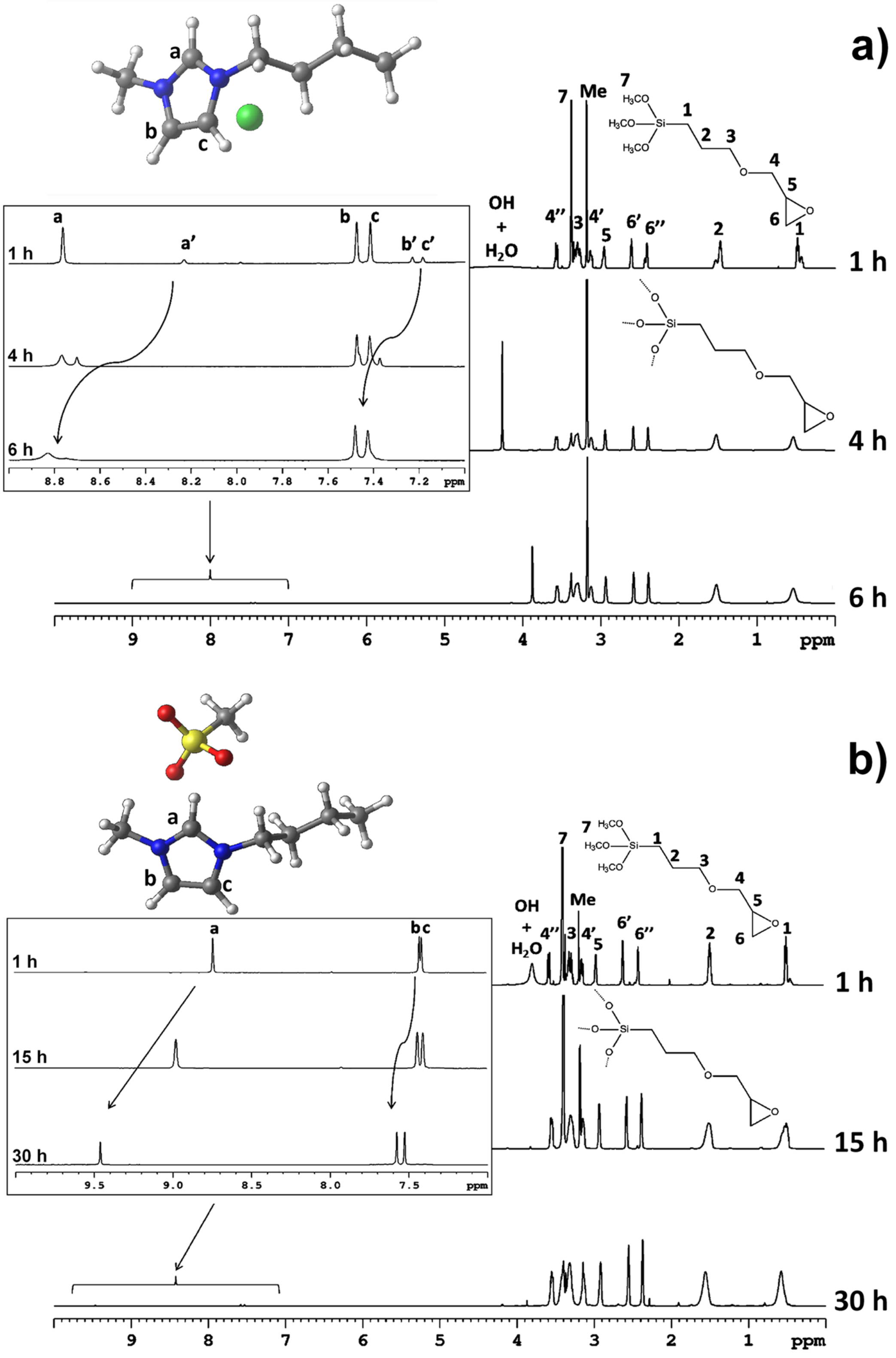

Figure 5. ^{1}H NMR spectra of the three time fractions collected during (a) C_4MImCl− and (b) C_4MImMeSO$_3$−silica sol−gel process.

similar silica structures. The right deconvoluted peak (Figure 4, peak 4) was positioned at q = 4.31 nm^{-1} and corresponded to the 1.46 nm distance. Such results suggested formation of POSS silica structures with cage-to-cage distance of 1.46 and 1.59 nm, which correlates well with the modeled silica structures (Figure 3) and previously described ^{29}Si MAS NMR results (Table 2).

In summary, the integration of all results (^{29}Si NMR, SAXS, MALDI TOF, etc.) allowed us to conclude that both ILs caused formation of a similar set of silica structures but in different proportions. The C_4MImCl promoted a faster sol−gel process

Scheme 1. Proposed Hydrolyzed Siloxane Stabilization Mechanism Showing the Initial Hydrolysis Step (a) and the Most Stable Relaxed Structures (Presenting the Most Intimate Interatomic Distances and Stronger Binding Energies Obtained by DFT) of the Hydrolyzed Siloxane in the Presence of C_4MImCl (b and e) and $C_4MImMeSO_3$ (c and d)

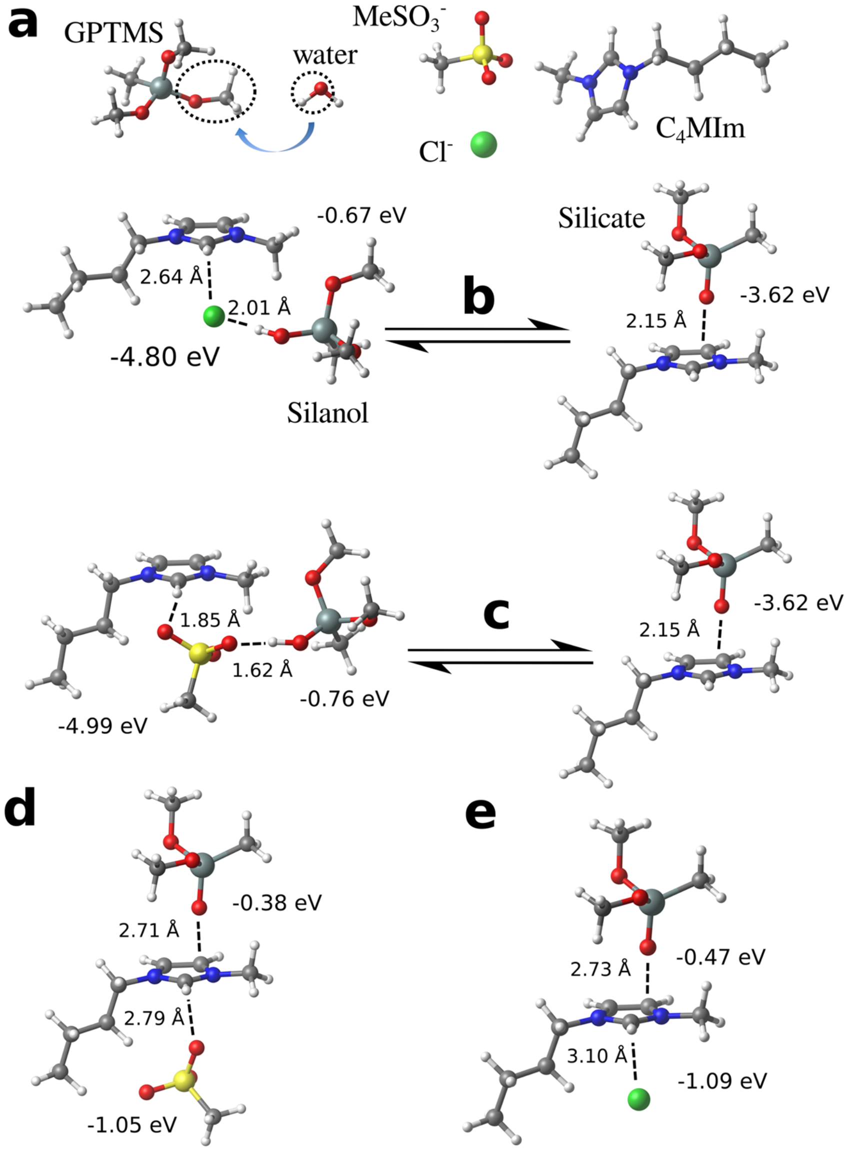

(Table 1); therefore, the formation of 3D cage-like silica structures prevailed. In this sense, C_4MImCl behaves similarly to the DABCO catalyst, as we described previously.[23] In the case of $C_4MImMeSO_3$-based system, the rate of sol−gel was significantly lower, and the final product exhibited just ∼74.4% of condensation degree after 30 h of reaction when the sol mixture probably reached some equilibrium. Therefore, it is likely that such behavior led to the higher storage stability of $C_4MImMeSO_3$−silica precursor and lower condensation degree of further xerogel. Importantly, the silica structures predicted by DFT simulations correlated well with these assumptions.

3.2. IL-Driven Sol−Gel Mechanism. Detailed analysis of FTIR spectra collected during the sol−gel synthesis of IL−silica precursors allowed detection of the different influences of IL anions on the hydrolytic polycondensation reaction (Figure S5a and b). The C_4MImCl−silica sol−gel system showed a faster polycondensation step compared to the one with $C_4MImMeSO_3$, as a large number of condensed silica structures formed in the Si−O−Si region (900−1200 cm^{-1}) after 2 h of sol−gel. In contrast, in the $C_4MImMeSO_3$−silica system, the Si−O−Si structures did not form even after 3 h of the sol−gel process (compare Figure S5a and b).

To better explain the mechanism of IL-driven sol−gel process, high-resolution ^1H NMR spectra were collected during the synthesis of IL−silica precursors at three different reaction times and under the same instrumental conditions (Figure 5a and b). The chemical structure of GPTMS and assignments of peaks corresponding to various protons were shown in each spectrum and were in agreement with the literature.[49]

The spectra showed that the epoxy rings remained unaltered in both IL−silica precursors (unchanged signals **6′** and **6″** at δ = 2.61 and 2.42 ppm) (Figure 5a and b). As we can observe from the spectrum of C_4MImCl−silica precursor (Figure 5a), -OCH_3 groups attached to silicon atoms at δ = 3.39 ppm (**7**) were already in the hydrolyzed form (formation of −OH groups, as evidenced by the disappearance of signal **7**) after 4 h of reaction. Moreover, after 1 h of hydrolysis at room temperature, each of the imidazolium ring's hydrogens presented two different peaks (a−a′, b−b′, and c−c′), suggesting the formation of two different types of interactions. We assumed that the signals with lower intensities (a′, b′, and c′) resulted from multiple H-bonding between the imidazolium ring's hydrogens and Cl anion,[50,51] which decrease during the sol−gel reaction (shift of a′, b′, and c′ peaks to lower field; Figure 5a) as a consequence of the increasing H-bonding between Cl^- and forming silanols. Therefore, the more intensive a, b, and c peaks might correspond to the H-bond interactions between the imidazolium ring's hydrogens, Cl anion, and −OH groups from hydrolyzed GPTMS, water, and methanol (Figure 5a),[52−56] as similar signals were also detected in the ^1H NMR spectra of neat C_4MImCl in methanol (Figure S6a). Importantly, during the polycondensation step at 80 °C, the detected a′, b′, and c′ peaks shifted to lower field, probably due to the formation of silanol and methanol and their subsequent interactions with IL. However, a slight shift of peak "a" to lower field after 6 h of polycondensation might indicate the formation of a silicate anion stabilized by the positively charged imidazolium ring (Scheme 1b).

In contrast, in the $C_4MImMeSO_3$−silica system, the -OCH_3 groups were not fully hydrolyzed even after 15 h of reaction (Figure 5b). Therefore, the amount of formed methanol ("Me" peak at $\delta = 3.19$ ppm) was much lower than that in the case of C_4MImCl-catalyzed sol−gel system. The visible reduction in the OH+H_2O peak intensity could be caused by the formation of protonic acid ($HMeSO_3$), as described in the literature.[33] Importantly, after 1 h of hydrolysis at room temperature, the $C_4MImMeSO_3$−silica system did not show the two different peaks of each imidazolium proton (Figure 5b), as detected in the C_4MImCl−silica system (Figure 5a). Also, the NMR spectra of pure $C_4MImMeSO_3$ in methanol showed just the peaks a, b, and c (Figure S6b). Such difference might be caused by the formation of stronger H-bonding between imidazolium ring's hydrogens and $MeSO_3^-$ (−4.99 eV), compared to the Cl^- (−4.80 eV), as well as the smaller distance between imidazolium ring and $MeSO_3^-$ (1.85 A), reducing the $MeSO_3^-$ mobility and subsequently the number of formed H-bonding interactions with the imidazolium ring (Scheme 1). Therefore, we assumed that the detected a, b, and c peaks (Figure 5b) most probably corresponded to the interactions between imidazolium ring's hydrogens, $MeSO_3$ anion, and other sol−gel components (silanol, water, and methanol). Moreover, the mentioned a, b, and c peaks shifted during the sol−gel process to a lower field, which might be affected by partial evaporation of methanol from the reaction mixture (long synthesis time: 30 h; Table 1), leading to changes in H-bonding as well as by the different reaction mechanism between the imidazolium ring and formed silicate (Scheme 1c).

The capacity of ILs to strongly interact with hydrolyzed siloxanes and influence the silica condensation step is well-known, even in complex systems.[6,38] However, the positively charged imidazolium ring is also able to stabilize a silicate anion, which can be formed even at pH < 7.[57] Considering that our sol−gel processes are performed at pH ∼ 5.5, both the neutral silanols and negatively charged silicate anions could coexist during the evolution of the system. Because silanols interact with ILs via H-bonding and silicates interact with ILs via Coulomb interactions, different electron densities could be expected for the imidazolium cation in each case, which might correspond, respectively, to the chemical shifts of a, b, and c peaks in NMR spectra and their further shift to the lower field due to the appearance of silicate−IL interactions during the sol−gel process (Figure 5a and b).

To calculate the most energetically favorable species forming in the IL−silica sol−gel systems, DFT simulations were performed, acquiring both the closest interatomic distances and the binding energies between species. When evaluating the H-bond formation between silanols and the ILs, $MeSO_3^-$ shows a stronger H-bonding (−0.76 eV) when compared to Cl^- (−0.67 eV), probably due to the smaller bond size (1.62 Å) (Scheme 1b and c). This could be why only a, b, and c peaks were detected in the NMR spectra after 1 h of hydrolysis at room temperature (Figure 5b). Moreover, considering the hydrogen loss of silanol and subsequent formation of a silicate and the IL anion's conjugated acid,[57] a quite stable silicate−imidazolium ion pair might be produced (−3.62 eV; Scheme 1b and c). The formation of imidazolium-stabilized species could retard the sol−gel condensation step in the $C_4MImMeSO_3$−silica system. Most probably, the formation of silicate−imidazolium ion pair is dependent on the stability of the IL anions' conjugated acid because they are also formed in the process. $C_4MImMeSO_3$ forms the weaker and less reactive methanesulfonic acid ($HMeSO_3$, $pK_a = 1.92$) compared to hydrochloric acid (HCl, $pK_a = 6.3$) formed from C_4MImCl.[58,59]

Furthermore, the mechanisms in which the IL and silicate anions simultaneously influence the 1-butyl-3-methylimidazolium cation were also evaluated (Scheme 1d and e). However, the formed species presented very weak binding energies and were therefore too unstable and short-lived to influence the sol−gel process.

3.3. Epoxy−Silica Hybrid Materials.

SAXS curves of hybrid materials with the highest content (22 wt %) of IL−silica precursors displayed slightly different profiles, depending on the SiO_2 presence and type of IL anion (Figure 6). A strong correlation peak at $q = 4.5$ nm^{-1} present in the matrix, corresponding to the distance $d = 2\pi/q = 1.43$ nm of the poly(oxypropylene)diamine packing sequences,[8,10] remained at same position and was not dependent on the IL type (Figure 6). This meant that the addition of IL−silica precursor in a high amount (22.0 wt %) did not change the regularities in the matrix network, as previously detected.[10] The higher intensity in the middle q-region resulted from the increased electron density due to incorporation of inorganic component. The scattering curves of both hybrids containing the C_4MImCl− and $C_4MImMeSO_3$−silica precursors comprised a traditional cross-linked network behavior, which, together with the absence of other features in the low- and middle-q region, indicated homogeneity of the system and thus could be a sign

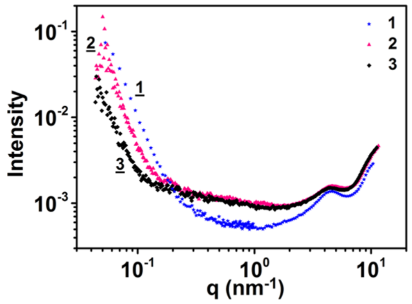

Figure 6. SAXS patterns of the reference epoxy−amine matrix (1) and synthesized hybrid materials containing 22.0 wt % of the C_4MImCl− (2) and $C_4MImMeSO_3$−silica precursor (3).

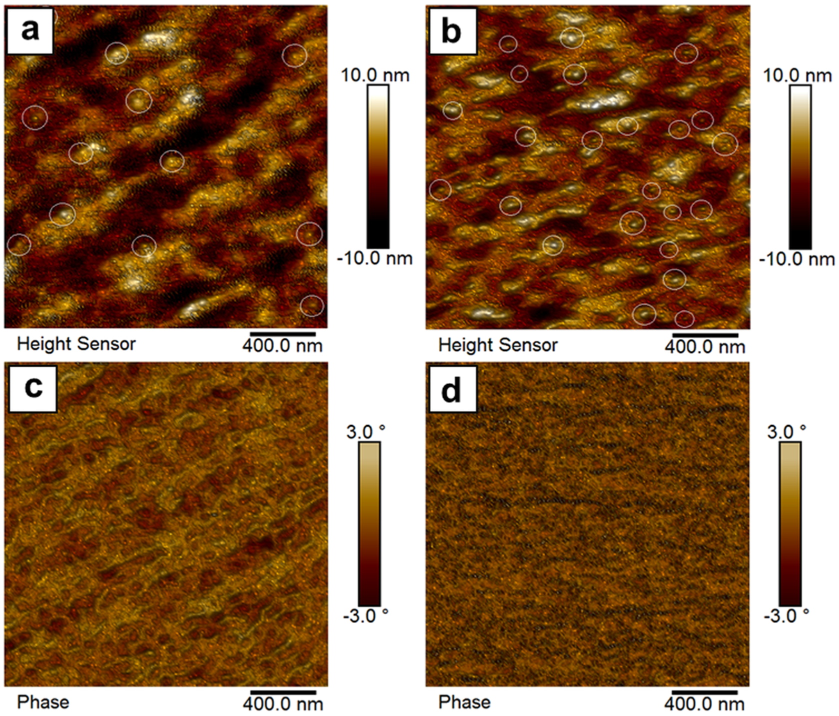

Figure 7. AFM 3D height (a and b) and phase (c and d) diagrams of the DGEBA-D-230-C_4MImCl(6.8) (a and c) and DGEBA-D-230-C_4MImMeSO$_3$(6.8) hybrids (b and d) (silica aggregates are highlighted with a circle).

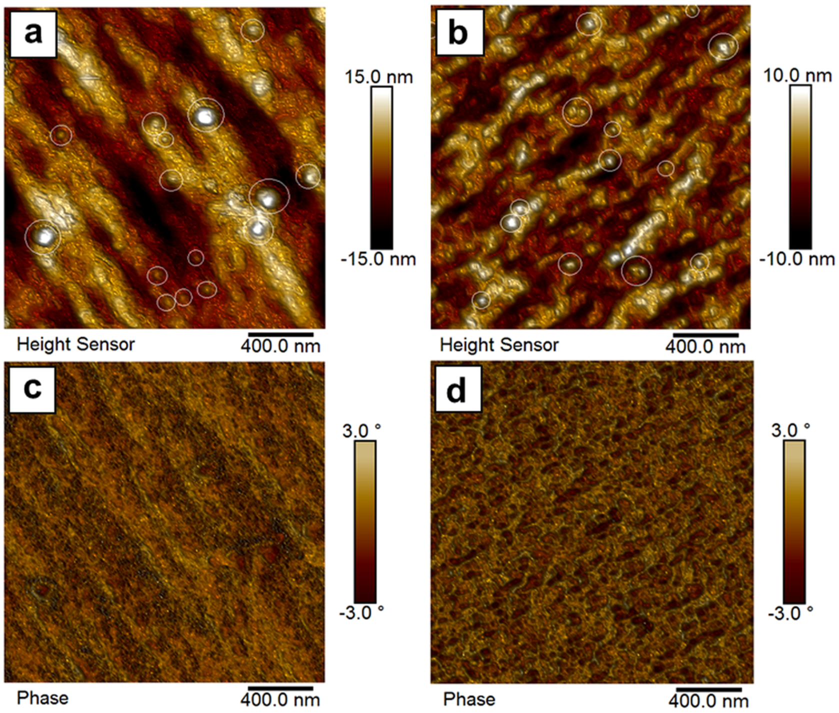

Figure 8. AFM 3D height (a and b) and phase (c and d) diagrams of DGEBA-D-230-C_4MImCl(22.0) (a and c) and DGEBA-D-230-C_4MImMeSO$_3$(22.0) hybrids (b and d) (silica aggregates are highlighted with a circle).

of rather good adhesion between DGEBA-D230 and the silica structures. The incorporation of silica species increased the inter-cross-link distance, resulting in a scattering curve shift to lower angles ($0.04 < q < 0.2$ nm^{-1}). The intensity in this region falls faster in the case of hybrid with C_4MImCl—silica precursor, which could be the result of signal superposition between matrix and silica aggregates. A clear form factor could not be calculated, disabling the conclusion about the aggregate's morphology. Nevertheless, the subtraction of a curve with the same slope as we observe in the matrix resulted in a peak at $q \sim 0.053$ nm^{-1}, corresponding to the correlation distance of 118 nm. The observed result was in agreement with AFM images (see later Figure 7).

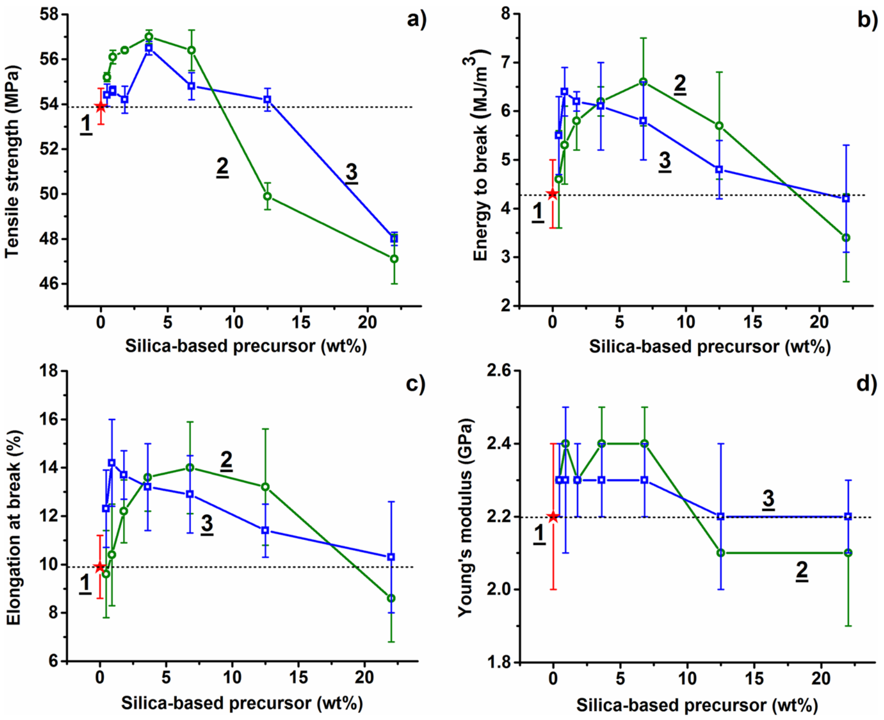

Figure 9. Room-temperature tensile properties of the reference epoxy−amine matrix (1) and the epoxy−silica hybrid materials containing different amounts of the C_4MImCl− (2) and $C_4MImMeSO_3$−silica (3) precursors: (a) tensile strength, (b) energy to break, (c) elongation at break, and (d) Young's modulus.

The AFM 3D phase and height diagrams of the reference DGEBA-D-230 matrix and epoxy−silica hybrids containing 6.8 or 22.0 wt % of IL−silica precursor are shown in Figure S7 and Figure 7, respectively. Nevertheless, the differences could be mainly observed in the height profiles (Figure 7a and b and Figure 8a and b). The phase diagrams, which provide contrast between hard silica particles and soft polymer, were used to examine the compatibility of hybrid materials. No defined contrast between organic and inorganic components was observed in the phase profiles (Figure 7c and d and Figure 8c and d), signifying improved interphase interactions and final adhesion between silica and the epoxy matrix compared to our previous results.[10] It was observed that independently on the silica structures present in the admixed IL−silica precursors (cages, ladders, cycles, etc.), spherical inorganic−organic inclusions were formed.

In the case of DGEBA-D-230-C_4MImCl(6.8) and DGEBA-D-230-$C_4MImMeSO_3$(6.8), the visible particles had regular shape in all directions and average size of 30 nm (Figure 7a and b). It was clearly visible for both samples that the silica particles were quite well-dispersed in the matrix, which could be influenced by the presence of ILs. Nevertheless, the accurate size of silica particles could not be established, as the detected inclusions corresponded to the silica species covered by the organic phase (see lack of phase contrast in Figure 7c and d). Importantly, such homogeneously spread silica species caused high transmittance of hybrid materials in UV−vis region. The addition of IL−silica precursors improved even the transparency of reference matrix in UV region, as the UV absorption at 350 nm was reduced to 25% compared to that of the matrix (∼38%; Figure S8). Such behavior was probably the result of high compatibility between silica structures and epoxy−amine network, additionally enhanced by IL.

In contrast, the DGEBA-D-230-C_4MImCl(22.0) and DGEBA-D-230-$C_4MImMeSO_3$(22.0) hybrids contained larger aggregates due to the higher silica content.[23] Nevertheless, the lack of contrast between inorganic silica and organic DGEBA-D-230 matrix in phase profiles (Figure 8c and d) indicated good interphase adhesion, much more improved compared to the previously described IL-free epoxy−silica hybrids with conventional catalysts.[19] The well-ordered aggregates observed in the DGEBA-D-230-C_4MImCl(22.0) hybrid system had lateral sizes ranging from 50 to 125 nm and were larger than previously reported (Figure 8a).[10] These inclusions did not significantly influence the optical transparency of hybrid, which was comparable to that of the reference matrix (Figure S8a). In contrast, the DGEBA-D-230-$C_4MImMeSO_3$(22.0) hybrid contained smaller spherical silica aggregates with lateral dimensions of 30−80 nm (Figure 8b), which were highly compatible with the organic matrix and contributed to the increase in UV transmittance of the final hybrid material (Figure 8b).

The tensile properties of the glassy epoxy−amine matrix and epoxy−silica hybrid materials containing different amounts of IL−silica precursors are demonstrated in Figure 9. The neat epoxy−amine matrix presented a low energy to break (∼4.3 MJ/m^3) and high Young's modulus (∼2.2 GPa), typical for brittle epoxides.[10] Moreover, the elongation at break reached only ∼10% due to the high cross-linking density of the matrix. The addition of IL−silica precursors did not significantly change the Young's modulus of the epoxy−silica hybrid materials; however, the tensile properties were considerably affected when compared to the reference DGEBA-D-230 matrix (Figure 9d).[7,10] The highest improvement in tensile properties was obtained for the hybrids containing 3.6−6.8 wt % of C_4MImCl−silica precursor (Figure 9 and Table S3), revealing an increase in the tensile strength, energy to break, and

Table 3. Thermal and Mechanical Properties of Reference Epoxy–amine Matrix and Epoxy–silica Hybrid Materials

	sample	IL–silica precursor (wt %)	amount of IL (wt %)	T_α (°C)	G_R' (MPa)[a]	$T_{10\%}$ (°C)[b]	solid residue (wt %)[c]	Si (wt %)[d]	SiO_2 (wt %)[e]
1	DGEBA-D-230			95	12.9	366	0.0	0.0	0.0
2	DGEBA-D-230-C_4MImCl	0.5	0.004	95	23.8	386	0.2	0.1	0.2
3		0.9	0.008	95	27.3	389	0.7	0.3	0.6
4		1.8	0.016	96	28.3	391	0.8	0.6	1.3
5		3.6	0.032	95	31.5	390	1.4	1.1	2.4
6		6.8	0.061	95	35.3	383	2.4	2.2	4.7
7		12.5	0.113	92	48.6	385	4.2	3.8	8.1
8		22.0	0.197	91	63.4	386	7.2	5.8	12.4
9	DGEBA-D-230-C_4MImMeSO_3	0.5	0.004	96	25.6	392	0.4	0.2	0.4
10		0.9	0.008	95	26.3	385	0.5	0.3	0.6
11		1.8	0.016	96	28.2	385	0.8	0.6	1.3
12		3.6	0.032	96	30.8	388	1.3	1.2	2.6
13		6.8	0.061	95	34.1	386	2.8	2.0	4.3
14		12.5	0.113	93	43.1	385	3.8	3.7	7.9
15		22.0	0.197	92	52.1	379	7.0	5.8	12.4

[a] At 150 °C. [b] Temperature of 10% weight loss. [c] As obtained by TGA (air) at 860 °C. [d] Si content determined by XRF. [e] The equivalent of SiO_2 calculated from the Si (wt %) obtained by XRF.

elongation at break up to ~7, ~ 53, and ~41%, respectively. In the case of DGEBA-D-230-C_4MImMeSO_3 hybrid system, only 0.9–3.6 wt % of IL–silica precursor was necessary for obtaining similar improvement in tensile properties (Figure 9 and Table S3). Such results indicated the better incorporation and compatibility of the C_4MImMeSO_3–silica structures with the epoxy–amine network as well as the formation of much smaller silica domains in the final hybrid, offering a larger matrix–filler interphase area. In comparison, we previously used the same epoxy matrix for the in situ nonhydrolytic sol–gel preparation of epoxy–silica hybrids exhibiting similar elongation at break (~47%) but only ~2 and ~29% increase in tensile strength and toughness, respectively, with a much higher amount of silica applied (7.5 wt %)[7] (compare to results in Table 3 and Table S3).

Moreover, the applied imidazolium-based ILs reduced the silica aggregation and improved O/I interphase interactions and silica dispersion compared to the conventional sol–gel catalysts described before (Figures 7 and 8).[10] The mutual interactions between silica structures, IL, and organic network chains also strongly influenced the elastic deformation and stress transfer from the matrix to the filler. In general, the inorganic particles hinder crack propagation, absorbing stresses accumulated or transmitted through the organic matrix.[60] Thus, the improvement in tensile strength (Figure 9a) might be a result of synergistic physical-covalent matrix/filler interphase bonding, significantly improving the O/I interphase adhesion. The poorest tensile properties exhibited both epoxy–silica hybrid materials with 22.0 wt % of IL–silica precursors (Figure 9 and Table S3), which was a consequence of the network saturation and silica aggregation, as confirmed by AFM (Figure 8).

The main thermomechanical properties of epoxy–silica hybrid materials, including the α-relaxation temperature (T_α), storage (G'), and loss (G'') shear moduli, were evaluated using DMTA (Table 3 and Figure S9). The addition of small amounts of IL–silica precursors (≤6.8 wt %) into the epoxy–amine network did not influence T_α of hybrid materials (Table 3), suggesting that at this amount the precursors did not significantly affect the network free volume. However, the higher precursor loadings (≥12.5 wt %) led to a slight decrease in T_α, caused probably by both the IL presence and the increased size of silica aggregates (Figure 7 and Figure 8). The drop in the loss factor (tan δ) peak intensity, reflecting the reduction in polymer chain mobility, was similar in both systems and did not strongly depend on the amount of added IL–silica precursors (Figure S9). Such behavior signifies that the epoxy–amine matrix contribution in the relaxation process was strongly decreased, even when small amounts (≤6.8 wt %) of IL–silica precursors were added. Thus, the presence of ILs and silica inclusions most probably immobilized the epoxy–amine network.[10,61−63] The higher precursor loadings (22.0 wt %) led to the significant decrease in height of tan δ peak (especially in the DGEBA-D-230-C_4MImCl(22.0) system) as a consequence of segmental mobility reduction caused by the presence of higher amount of inorganic inclusions and incorporated IL, which could also slightly plasticize the hybrid system (Figure 8a and Figure S9).[10,61−63] Importantly, with the increasing amount of added silica-based precursor, the IL content in the final hybrid material also increased (Table 3).

The rubbery shear storage moduli (G_R') of all hybrids were significantly improved compared to those of the reference matrix due to the nanofiller reinforcing effect and increased cross-linking density (Table 3 and Figure S9). Such behavior was a consequence of both chemical and physical bonding at the O/I interphase, synergistically generated by the functional glycidyloxypropyl chains of silica particles and ILs.

To compare, Ponyrko et al.[8] obtained epoxy–silica hybrid materials using the in situ nonhydrolytic sol–gel process, which exhibited lower values of G_R' (<50 MPa) and significantly decreased T_α (even for about 32 °C), even when much higher amount of silica (~10 wt %) was applied (see Table 3 and Table S3). Furthermore, the same group presented a modified in situ nonhydrolytic sol–gel method,[9] which lead to the improvement in T_α of the final hybrids (for about 20 °C) containing, nevertheless, much higher silica content (~10 wt %). In contrast, Piscitelli et al.[64] reported the synthesis of epoxy–silica hybrids using a two-step procedure, leading to significant increase in G_R' (~20 times) and T_α (~15 °C) but only at very high silica loadings (~22 wt %). The hybrid containing ~7 wt % of silica (comparable with our system) did not exhibit any change in T_α, and the obtained G_R' values were lower (~30 MPa) compared to those of our hybrid materials.

DOI: 10.1021/acsami.7b02631
ACS Appl. Mater. Interfaces 2017, 9, 16474−16487

Moreover, we previously reported the preparation method of epoxy−silica hybrids using the conventionally catalyzed ex situ sol−gel process, which led to the high improvement in G_R' and caused insignificant decrease in T_α but only at higher silica loadings (e.g., for ∼11 wt % of silica G_R' ∼56 MPa and T_α decreased only ∼8 °C).[10] Therefore, concerning the thermal and mechanical properties of hybrids, we assumed that the incorporation of IL−silica precursors into the DGEBA-D-230 matrix was evidently much more effective than the addition of silica prepared without ILs.

TGA showed that the initial 10% weight loss ($T_{10\%}$) of all hybrids shifted to higher temperatures when compared to the reference matrix (Figure S10 and Table 3). The first main weight loss (300−500 °C) corresponded to the decomposition of organic matrix, IL, and glycidyloxypropyl side chains of silica structures.[3,10,65−67] Subsequently, the products formed during the first step of thermal decomposition underwent oxidative degradation in the second weight-loss step, which was significantly shifted to higher temperatures with increasing silica content (Figure S10). Thus, the well-dispersed hard silica species acted as a barrier against heat and oxygen transport, resulting in the improved thermooxidative stability of hybrids.[65,68,69] The exact silica contents (theoretical SiO_2 wt %) in the hybrid materials were determined by the recalculation of Si wt % values obtained by XRF (Table 3), which allowed better comparison with the amount of solid residues formed during thermooxidative treatment of hybrids (Table 3). We observed that at higher IL−silica precursor loadings (>1.8 wt %), the experimental silica contents (obtained by TGA) were significantly lower than the theoretical ones obtained from XRF (Table 3), which might be caused by the sublimation of less thermally stable silica structures.[10,64,70]

4. CONCLUSIONS

The ILs applied to the sol−gel process allowed us to obtain highly condensed IL−silica precursors with distinguished and controllable morphologies and rheological behavior. The C_4MImCl caused the predominant formation of three-dimensional cage-like silica structures (q ∼ 90%) in the final precursor, which converted to xerogel with q ∼ 100%. In contrast, the $C_4MImMeSO_3$ led to a precursor with more varied but predominantly more planar silica structures, e.g., partially opened cages, ladders, and cycles, forming a 96% condensed xerogel.

The sum of experimental and theoretical evaluations revealed that the precursor characteristics were driven by interactions between the imidazolium ring, anion, and the evolving silicon species. The faster sol−gel process driven by C_4MImCl, leading to the formation of defined 3D silica structures (cages), was influenced by the higher mobility of Cl anion that created weaker H-bonding with imidazolium protons and interacted more intensively with the forming silanols. However, the $MeSO_3$ anion presented both stronger bonding with the cation and an apparent higher tendency to form silicate species which strongly bind to the imidazolium cation, affecting the silica structure evolution. This led to the formation of less condensed partially opened cages and ladder-like structures.

The prepared IL−silica precursors exhibited good storage stability and could be easily admixed into epoxy prepolymers, producing homogeneously dispersed epoxy−silica hybrid materials. Accordingly, the samples containing ∼6.8 wt % of C_4MImCl− or $C_4MImMeSO_3$−silica precursors exhibited similar morphology, characterized by the small, regularly shaped and homogeneously spread silica aggregates in the size of ∼30 nm. Moreover, the use of ILs in these systems clearly led to an improvement in interphase bonding, as witnessed by the lack of contrast in AFM phase profiles and SAXS curves.

Even small amounts (≤6.8 wt %) of IL−silica precursors immobilized the epoxy−amine network and strongly decreased the contribution of the matrix in the relaxation process. The shear storage modulus was significantly improved (up to 5 times) due to the reinforcing nanofiller effect and increasing cross-linking density. Interestingly, the less-condensed precursor with $C_4MImMeSO_3$ was 7 times more effective in reinforcing the matrix than the C_4MImCl−silica precursor, as only 0.9 wt % of the first and 6.8 wt % of the latter was necessary for obtaining a ∼50% increase in the energy to break and 40% increase in the elongation at break. Importantly, all hybrids showed unaltered optical transparency, reduced UV absorption tendency (to ∼25%), and improved thermooxidative stability, which make IL−silica precursors (especially with $C_4MImMeSO_3$) outstanding multifunctional additives for epoxy networks. The prepared epoxy−silica hybrid materials are proposed to be used in industry for casting and encapsulation of electronic devices, light-emitting diodes, and other optical elements.

■ ASSOCIATED CONTENT

Supporting Information

The Supporting Information is available free of charge on the ACS Publications website at DOI: 10.1021/acsami.7b02631.

^{1}H NMR spectra, DSC results, TGA and DTG curves of neat ILs; ^{29}Si NMR, FTIR, and MALDI TOF mass spectra of IL−silica precursors; silica structures detected in the MALDI TOF mass spectra of IL−silica precursors; ^{29}Si MAS NMR spectra of silica xerogels; AFM images, UV−vis spectra, tensile properties, and DMTA and TGA curves of epoxy−silica hybrids (PDF)

■ AUTHOR INFORMATION

Corresponding Author

*Phone: +420 296 809 390; Fax: +420 296 809 410; E-mail: perchacz@imc.cas.cz.

ORCID

Magdalena Perchacz: 0000-0002-1803-7771

Notes

The authors declare no competing financial interest.

■ ACKNOWLEDGMENTS

This work was supported by the Czech Science Foundation (Project 17-08273S) and the Ministry of Education, Youth and Sports of CR (Project POLYMAT LO1507). M.P. acknowledges the Charles University, Faculty of Science, for the opportunity to pursue her Ph.D. study. The authors thank Ms. Zuzana Walterová for the MALDI TOF analysis and Olga Trhlíková, Ph.D. for the XRF analysis. R.K.D. and L.S. acknowledge FAPESP (SPEC Project 2012/50259-8) for financial support and the Centre for Advanced 2D Materials and Graphene Research Centre, National University of Singapore for high-performance computational facilities.

■ ABBREVIATIONS

C_4MImCl, 1-butyl-3-methylimidazolium chloride

$C_4MImMeSO_3$, 1-butyl-3-methylimidazolium methanesulfonate
D-230, poly(oxypropylene)diamine, Jeffamine D-230
DABCO, 1,4-diazabicyclo[2.2.2]octane
DGEBA, diglycidylether of bisphenol A, D.E.R. 332
GPTMS, (3-glycidyloxypropyl)trimethoxysilane
POSS, polyhedral oligosilsesquioxane

REFERENCES

(1) Matějka, L.; Dukh, O.; Kolařík, J. Reinforcement of Crosslinked Rubbery Epoxies by In-situ Formed Silica. *Polymer* **2000**, *41*, 1449−1459.

(2) Matějka, L.; Strachota, A.; Pleštil, J.; Whelan, P.; Steinhart, M.; Šlouf, M. Epoxy Networks Reinforced with Polyhedral Oligomeric Silsesquioxanes (POSS). Structure and Morphology. *Macromolecules* **2004**, *37*, 9449−9456.

(3) Beneš, H.; Galy, J.; Gérard, J. F.; Pleštil, J.; Valette, L. Preparation and Characterization of Organic/Inorganic Hybrid Epoxy Networks from Reactive Inorganic Precursors. *J. Appl. Polym. Sci.* **2012**, *125*, 1000−1011.

(4) Lu, S. R.; Zhang, H. L.; Zhao, C. X.; Wang, X. Y. Preparation and Characterization of Epoxy-Silica Hybrid Materials by the Sol-Gel Process. *J. Mater. Sci.* **2005**, *40*, 1079−1085.

(5) Donato, R. K.; Matějka, L.; Schrekker, H. S.; Pleštil, J.; Jigounov, A.; Brus, J.; Šlouf, M. The Multifunctional Role of Ionic Liquids in the Formation of Epoxy-Silica Nanocomposites. *J. Mater. Chem.* **2011**, *21*, 13801−13810.

(6) Donato, R. K.; Donato, K. Z.; Schrekker, H. S.; Matějka, L. Tunable Reinforcement of Epoxy-Silica Nanocomposites with Ionic Liquids. *J. Mater. Chem.* **2012**, *22*, 9939−9948.

(7) Donato, R. K.; Perchacz, M.; Ponyrko, S.; Donato, K. Z.; Schrekker, H. S.; Beneš, H.; Matějka, L. Epoxy-Silica Nanocomposite Interphase Control Using Task-Specific Ionic Liquids via Hydrolytic and Non-Hydrolytic Sol−Gel Processes. *RSC Adv.* **2015**, *5*, 91330.

(8) Ponyrko, S.; Kobera, L.; Brus, J.; Matějka, L. Epoxy-Silica Hybrids by Nonaqueous Sol-Gel Process. *Polymer* **2013**, *54*, 6271−6282.

(9) Ponyrko, S.; Kovářová, J.; Kobera, L.; Matějka, L. High-Tg, Heat Resistant Epoxy-Silica Hybrids with a Low Content of Silica Generated by Nonaqueous Sol-Gel Process. *J. Appl. Polym. Sci.* **2014**, *131*, 20.

(10) Perchacz, M.; Beneš, H.; Zhigunov, A.; Serkis, M.; Pavlova, E. Differently-Catalyzed Silica-Based Precursors as Functional Additives for the Epoxy-Based Hybrid Materials. *Polymer* **2016**, *99*, 434−446.

(11) Meador, M. A. B.; Weber, A. S.; Hindi, A.; Naumenko, M.; McCorkle, L.; Quade, D.; Vivod, S. L.; Gould, G. L.; White, S.; Deshpande, K. Structure-Property Relationships in Porous 3D Nanostructures: Epoxy-Cross-Linked Silica Aerogels Produced Using Ethanol as the Solvent. *ACS Appl. Mater. Interfaces* **2009**, *4*, 894−906.

(12) Kickelbick, G. *Hybrid Materials: Synthesis, Characterization, and Applications*; Wiley-VCH Verlag GmbH & Co. KGaA: Weinheim, 2007.

(13) Serra, A.; Ramis, X.; Fernández-Francos, X. Epoxy Sol-Gel Hybrid Thermosets. *Coatings* **2016**, *6*, 8.

(14) Wang, Z.; Lv, Q.; Chen, S.; Li, C.; Sun, S.; Hu, S. Effect of Interfacial Bonding on Interphase Properties in SiO_2/Epoxy Nanocomposite: A Molecular Dynamics Simulation Study. *ACS Appl. Mater. Interfaces* **2016**, *8*, 7499−7508.

(15) Jiang, S. D.; Bai, Z. M.; Tang, G.; Song, L.; Stec, A. A.; Hull, T. R.; Hu, Y.; Hu, W. Z. Synthesis of Mesoporous Silica@Co−Al Layered Double Hydroxide Spheres: Layer-by-Layer Method and Their Effects on the Flame Retardancy of Epoxy Resins. *ACS Appl. Mater. Interfaces* **2014**, *6*, 14076−14086.

(16) Li, T.; Zhang, J.; Wang, H.; Hu, Z.; Yu, Y. High-Performance Light-Emitting Diodes Encapsulated with Silica-Filled Epoxy Materials. *ACS Appl. Mater. Interfaces* **2013**, *5*, 8968−8981.

(17) Legrand, A.; Soulié-Ziakovic, C. Silica-Epoxy Vitrimer Nanocomposites. *Macromolecules* **2016**, *49*, 5893−5902.

(18) Gómez-Romero, P.; Sanchez, C. *Functional Hybrid Materials*; Wiley-VCH Verlag GmbH & Co. KgaA: Weinheim, 2004.

(19) Pomogalio, A. D. Hybrid Polymer-Inorganic Nanocomposites. *Russ. Chem. Rev.* **2000**, *69*, 53−80.

(20) Letailleur, A. A.; Ribot, F.; Boissière, C.; Teisseire, J.; Barthel, E.; Desmazières, B.; Chemin, N.; Sanchez, C. Sol-Gel Derived Hybrid Thin Films: The Chemistry Behind Processing. *Chem. Mater.* **2011**, *23*, 5082−5089.

(21) Schottner, G. Hybrid Sol-Gel-Derived Polymers: Applications of Multifunctional Materials. *Chem. Mater.* **2001**, *13*, 3422−3435.

(22) Beneš, H.; Galy, J.; Gérard, J. F.; Pleštil, J.; Valette, L. Solvent-Free Synthesis of Reactive Inorganic Precursors for Preparation of Organic/Inorganic Hybrid Materials. *J. Sol-Gel Sci. Technol.* **2011**, *59*, 598−612.

(23) Perchacz, M.; Beneš, H.; Kobera, L.; Walterová, Z. Influence of Sol−Gel Conditions on the Final Structure of Silica-Based Precursors. *J. Sol-Gel Sci. Technol.* **2015**, *75*, 649−663.

(24) Hayes, R.; Warr, G. G.; Atkin, R. Structure and Nanostructure in Ionic Liquids. *Chem. Rev.* **2015**, *115*, 6357−6426.

(25) Ab Rani, M. A.; Brant, A.; Crowhurst, L.; Dolan, A.; Lui, M.; Hassan, N. H.; Hallett, J. P.; Hunt, P. A.; Niedermeyer, H.; Perez-Arlandis, J. M.; Schrems, M.; Welton, T.; Wilding, R. Understanding the Polarity of Ionic Liquids. *Phys. Chem. Chem. Phys.* **2011**, *13*, 16831−16840.

(26) Tariq, M.; Freire, M. G.; Saramago, B.; Coutinho, J. A. P.; Lopes, J. N. C.; Rebelo, L. P. N. Surface Tension of Ionic Liquids and Ionic Liquid Solutions. *Chem. Soc. Rev.* **2012**, *41*, 829−868.

(27) Li, H.; Bhadury, P. S.; Song, B.; Yang, S. Immobilized Functional Ionic Liquids: Efficient, Green, and Reusable Catalysts. *RSC Adv.* **2012**, *2*, 12525−12551.

(28) Vioux, A.; Viau, L.; Volland, S.; Le Bideau, J. Use of Ionic Liquids in Sol-Gel; Ionogels and Applications. *C. R. Chim.* **2010**, *13*, 242−255.

(29) Sheldon, R. Catalytic Reactions in Ionic Liquids. *Chem. Commun.* **2001**, *23*, 2399−2407.

(30) Olivier-Bourbigou, H.; Magna, L.; Morvan, D. Ionic Liquids and Catalysis: Recent Progress from Knowledge to Applications. *Appl. Catal., A* **2010**, *373*, 1−56.

(31) Dupont, J. On the Solid, Liquid and Solution Structural Organization of Imidazolium Ionic Liquids. *J. Braz. Chem. Soc.* **2004**, *15*, 341−350.

(32) Martinelli, A.; Nordstierna, L. An Investigation of the Sol-Gel Process in Ionic Liquid-Silica Gels by Time Resolved Raman and ^1H NMR Spectroscopy. *Phys. Chem. Chem. Phys.* **2012**, *14*, 13216−13223.

(33) Migliorini, M. V.; Donato, R. K.; Benvegnú, M. A.; Goncalves, R. S.; Schrekker, H. S. Imidazolium Ionic Liquids as Bifunctional Materials (Morphology Controller and Precatalyst) for the Preparation of Xerogel Silica's. *J. Sol-Gel Sci. Technol.* **2008**, *48*, 272−276.

(34) Pârvulescu, V. I.; Hardacre, C. Catalysis in Ionic Liquids. *Chem. Rev.* **2007**, *107*, 2615−2665.

(35) Betti, C.; Landini, D.; Maia, A. Reactivity of Anionic Nucleophiles in Ionic Liquids and Molecular Solvents. *Tetrahedron* **2008**, *64*, 1689−1695.

(36) Cammarata, L.; Kazarian, S. G.; Salter, P. A.; Welton, T. Molecular States of Water in Room Temperature Ionic Liquids. *Phys. Chem. Chem. Phys.* **2001**, *3*, 5192−5200.

(37) Koddermann, T.; Wertz, C.; Heintz, A.; Ludwig, R. The Association of Water in Ionic Liquids: A Reliable Measure of Polarity. *Angew. Chem., Int. Ed.* **2006**, *45*, 3697−3702.

(38) Zhou, Y.; Schattka, J. H.; Antonietti, M. Room-Temperature Ionic Liquids as Template to Monolithic Mesoporous Silica with Wormlike Pores via a Sol-Gel Nanocasting Technique. *Nano Lett.* **2004**, *4*, 477−481.

(39) Hohenberg, P.; Kohn, W. Inhomogeneous Electron Gas. *Phys. Rev.* **1964**, *136*, B864.

(40) Kohn, W.; Sham, L. J. Self-Consistent Equations Including Exchange and Correlation Effects. *Phys. Rev.* **1965**, *140*, A1133−A1138.

(41) Soler, J. M.; Artacho, E.; Gale, J. D.; García, A.; Junquera, J.; Ordejón, P.; Sánchez-Portal, D. The SIESTA Method for Ab Initio

Order-N Materials Simulation. *J. Phys.: Condens. Matter* **2002**, *14*, 2745−2779.

(42) Troullier, N.; Martins, J. L. Efficient Pseudopotentials for Plane-Wave Calculations. *Phys. Rev. B: Condens. Matter Mater. Phys.* **1991**, *43*, 1993−2006.

(43) Perdew, J. P.; Burke, K.; Ernzerhof, M. Generalized Gradient Approximation Made Simple. *Phys. Rev. Lett.* **1996**, *77*, 3865−3868.

(44) Brus, J. Heating of Samples Induced by Fast Magic-Angle Spinning. *Solid State Nucl. Magn. Reson.* **2000**, *16*, 151−160.

(45) Berger, S.; Braun, S. *200 and More NMR Experiments*; WILEY-VCH Verlag GmbH & Co. KGaA: Weinheim, 2004.

(46) Hook, R. J. A ^{29}Si NMR Study of the Sol-Gel Polymerisation Rates of Substituted Ethoxysilanes. *J. Non-Cryst. Solids* **1996**, *195*, 1−15.

(47) Raghavan, S. R.; Walls, H. J.; Khan, S. A. Rheology of Silica Dispersions in Organic Liquids: New Evidence for Solvation Forces Dictated by Hydrogen Bonding. *Langmuir* **2000**, *16*, 7920−7930.

(48) Itoh, M.; Oka, F.; Suto, M.; Cook, S. D.; Auner, N. Characterization and Some Insights into the Reaction Chemistry of Polymethylsilsesquioxane or Methyl Silicone Resins. *Int. J. Polym. Sci.* **2012**, *2012*, 1−17.

(49) Gabrielli, L.; Russo, L.; Poveda, A.; Jones, J. R.; Nicotra, F.; Jiménez-Barbero, J.; Cipolla, L. Epoxide Opening Versus Silica Condensation During Sol-Gel Hybrid Biomaterial Synthesis. *Chem. - Eur. J.* **2013**, *19*, 7856−7864.

(50) Hunt, P. A.; Gould, I. R. Structural Characterization of the 1-Butyl-3-Methylimidazolium Chloride Ion Pair Using Ab Initio Methods. *J. Phys. Chem. A* **2006**, *110*, 2269−2282.

(51) Hunt, P. A.; Ashworth, C. A.; Matthews, R. P. Hydrogen Bonding in Ionic Liquids. *Chem. Soc. Rev.* **2015**, *44*, 1257.

(52) Mele, A.; Tran, C. D.; De Paoli Lacerda, S. H. The Structure of a Room-Temperature Ionic Liquid with and without Trace Amounts of Water: The Role of C-H···O and C-H···F Interactions in 1-n-Butyl-3-Methylimidazolium Tetrafluoroborate. *Angew. Chem., Int. Ed.* **2003**, *42*, 4364−4366.

(53) Headley, A. D.; Jackson, N. M. The Effect of the Anion on the Chemical Shifts of the Aromatic Hydrogen Atoms of Liquid 1-Butyl-3-Methylimidazolium Salts. *J. Phys. Org. Chem.* **2002**, *15*, 52−55.

(54) Holbrey, J. D.; Seddon, K. R. The Phase Behaviour of 1-Alkyl-3-Methylimidazolium Tetrafluoroborates; Ionic Liquids and Ionic Liquid Crystals. *J. Chem. Soc., Dalton Trans.* **1999**, *13*, 2133−2139.

(55) Chakraborti, A. K.; Roy, S. R. On Catalysis by Ionic Liquids. *J. Am. Chem. Soc.* **2009**, *131*, 6902−6903.

(56) Dupont, J.; Suarez, P. A. Z.; De Souza, R. F.; Burrow, R. A.; Kintzinger, J.-P. C-H − π Interactions in 1-n-Butyl-3-Methylimidazolium Tetraphenylborate Molten Salt: Solid and Solution Structures. *Chem. - Eur. J.* **2000**, *6*, 2377−2381.

(57) Demadis, K. D.; Brückner, S. I.; Brunner, E.; Paasch, S.; Antonakaki, I.; Casolaro, M. The Intimate Role of Imidazole in the Stabilization of Silicic Acid by a pH-Responsive, Histidine-Grafted Polyampholyte. *Chem. Mater.* **2015**, *27*, 6827−6836.

(58) Guthrie, J. P. Hydrolysis of Esters of Oxy Acids: pKa Values for Strong Acids; Brønsted Relationship for Attack of Water at Methyl; Free Energies of Hydrolysis of Esters of Oxy Acids; and a Linear Relationship between Free Energy of Hydrolysis and pKa Holding Over a Range of 20 pK Units. *Can. J. Chem.* **1978**, *56*, 2342−2354.

(59) Jolly, W. L. *Modern Inorganic Chemistry*; McGraw-Hill: New York, 1984.

(60) Callister, Jr., W. D.; Rethwisch, D. G. *Materials Science and Engineering*, 8th ed; John Wiley & Sons Inc.: New York, 2010.

(61) Nazir, T.; Afzal, A.; Siddiqi, H. M.; Ahmad, Z.; Dumon, M. Thermally and Mechanically Superior Hybrid Epoxy-Silica Polymer Films via Sol-Gel Method. *Prog. Org. Coat.* **2010**, *69*, 100−106.

(62) Ochi, M.; Takahashi, R.; Terauchi, A. Phase Structure and Mechanical and Adhesion Properties of Epoxy/Silica Hybrids. *Polymer* **2001**, *42*, 5151−5158.

(63) Bugnicourt, E.; Galy, J.; Gérard, J. F.; Barthel, H. Effect of Sub-Micron Silica Fillers on the Mechanical Performances of Epoxy-Based Composites. *Polymer* **2007**, *48*, 1596−1605.

(64) Piscitelli, F.; Buonocore, G. G.; Lavorgna, M.; Verdolotti, L.; Pricl, S.; Gentile, G. Peculiarities in the Structure − Properties Relationship of Epoxy-Silica Hybrids with Highly Organic Siloxane Domains. *Polymer* **2015**, *63*, 222−229.

(65) Ahmad, Z.; Al-Sagheer, F. Novel Epoxy-Silica Nano-Composites Using Epoxy-Modified Silica Hyper-Branched Structure. *Prog. Org. Coat.* **2015**, *80*, 65−70.

(66) Li, Q.; Siddaramaiah, M. R.; Kim, N. H.; Hui, D.; Lee, J. H. Effects of Dual Component Microcapsules of Resin and Curing Agent on the Self-Healing Efficiency of Epoxy. *Composites, Part B* **2013**, *55*, 79−85.

(67) Dharaskar, S. A.; Varma, M. N.; Shende, D. Z.; Yoo, C. K.; Wasewar, K. L. Synthesis, Characterization and Application of 1-Butyl-3-Methylimidazolium Chloride as Green Material for Extractive Desulfurization of Liquid Fuel. *Sci. World J.* **2013**, *2013*, 1−9.

(68) Weng, W. H.; Chang, C. C.; Chen, H. Epoxy-Silica Hybrid Materials Synthesized via Sol-Gel Process. *Compos. Interfaces* **2005**, *11*, 631−641.

(69) Lu, S. R.; Zhang, H. L.; Zhao, C. X.; Wang, X. Y. Preparation and Characterization of Epoxy-Silica Hybrid Materials by the Sol-Gel Process. *J. Mater. Sci.* **2005**, *40*, 1079−1085.

(70) Tang, Y.; Lewin, M. Migration and Surface Modification in Polypropylene (PP)/Polyhedral Oligomeric Silsesquioxane (POSS) Nanocomposites. *Polym. Adv. Technol.* **2009**, *20*, 1−15.

■ NOTE ADDED AFTER ASAP PUBLICATION

This paper was published on the Web on May 2, 2017. Additional text corrections were implemented, and the paper was reposted on May 8, 2017.